

Investigation of the Trailing-Edge Jet-Buffer Phenomenon Using Circulation Control at Transonic Speeds

Dor Polonsky,*
Rafael© Advanced Defense Systems Ltd

The phenomenon of a periodic jet detachment occurring on an elliptic airfoil utilizing circulation control at transonic speeds was evaluated using numerical simulations. As the momentum of the jet increases beyond a prescribed magnitude, the jet begins to detach periodically from the surface of the trailing-edge. The effect was analyzed by both URANS calculations as well as by data-driven methods such as the Dynamic Mode Decomposition (DMD). The results of the investigation showed that the effect, termed jet-buffer is decoupled from the dominant shockwave located at the top surface of the wing. Indicating that the jet can no longer augment the wing's circulation, and thus the termination of circulation control. Furthermore, it was found that the driving mechanism of the jet-buffer originated from a feedback of pressure propagating between the trailing-edge shockwave and the downstream separation bubble produced by the jet. Consequently the jet-buffer causes noticeable fluctuations in the aerodynamic coefficients and such impacts the design implications of circulation-control at transonic flight.

I. Introduction

Control authority over aerial vehicles via active flow control (AFC) has garnered considerable attention, particularly through collaborations such as the 2010 DEMON [1, 2] and the 2018 MAGMA demonstrators, conducted jointly by BAE Systems and the University of Manchester [3, 4]. Similar efforts, including the DARPA-funded CRANE project [5], further highlight the growing interest in AFC due to its potential to enhance flight capabilities, as demands for vehicles of high maneuverability, endurance and range are on the rise. Recent research continues to expand AFC capabilities [6–10], reinforcing its viability in meeting these demands.

Among AFC methods, Circulation Control (CC), which relies on the injection of a Coandă jet [11], holds promise for flight maneuvering. By injecting the jet onto a rounded trailing-edge, centrifugal pressure forces the jet to attach to the surface, entraining surrounding air. This shifts the rear stagnation point along the trailing-edge curvature, increasing circulation and enhancing lift. These fluidic effectors are simple and aerodynamically efficient, capable of achieving high lift coefficients. However, their performance is constrained by airfoil design limitations, particularly regarding

*Aerodynamics & Fluid Mechanics Researcher, Rafael© Advanced Defense Systems Ltd, dmpwork0@gmail.com

trailing-edge radius and duct height [12]. Despite these constraints, the MAGMA demonstrator successfully utilized CC alongside Fluidic Thrust Vectoring as a primary maneuvering mechanism, even without strictly adhering to optimal design margins. This suggests that there remains significant potential for further exploration of CC design space.

For transonic speeds, CC implementation faces additional challenges. The presence of wave drag and potential shockwave buffets [13], the requirement for higher jet velocities to achieve meaningful effects [14], and the limited number of experimental studies compared to subsonic conditions [15–18] underscore the need for robust numerical validations. Research into transonic gust load alleviation [19], shape optimization [20], and CC aerodynamics for supercritical airfoils [21–23] has demonstrated the potential of CC at these conditions.

Currently, transonic CC numerical research primarily relies on steady jet blowing. For a steady jet, its momentum, expressed as the momentum coefficient must be high enough to prevent premature jet separation. However, detachment behavior is not always consistent across different designs, particularly when using an elliptic trailing-edge, shown in early work by Englar [24] to be favorable for transonic speeds. Experimental results by Alexander [15] revealed that in some cases, jet separation is not immediate but is preceded by a lift plateau. Numerical validations of this behavior [19, 21] indicate that attempting to maintain a steady jet within this plateau region leads to unsteadiness in both residuals and aerodynamic coefficients.

This study will show that the observed lift plateau is a consequence of periodic jet separation and reattachment. This periodic behavior can be numerically captured and analyzed using advanced data-driven methods. Proper Orthogonal Decomposition (POD) [25] enables the decomposition of the flow-field into its dominant coherent structures, while Dynamic Mode Decomposition (DMD) [26] projects these structures onto linearized dynamic modes, facilitating a deeper understanding of unsteady dynamics. These techniques have been extensively used to analyze periodic motion in transonic flows [27–29], allowing for the identification of key flow features and a more comprehensive study of periodic detachment behavior.

DMD itself is derived by projecting POD modes, obtained through Singular Value Decomposition (SVD), onto the Fourier space. This technique effectively identifies low-rank structures within the data [25]. Since DMD is purely data-driven, it does not require prior knowledge of system dynamics but relies on high-resolution, deterministic data, a requirement linked to its foundation in Koopman operator theory [30]. This constraint on time resolution can, however, be relaxed through sparsity-promoting methods such as compressive sensing [31].

Since unsteady periodic motion can induce responses in aerodynamic forces as well as structural fatigue effects via aeroelastic coupling [32], understanding the periodic detachment can impact transonic CC design methodologies. Thus, this study aims to introduce and characterize the phenomenon, termed jet-buffet, elaborate on its underlying mechanisms, and assess its implications for circulation control.

The paper is structured as follows: Section II details the geometry of the model used for calculations, followed by the numerical setup in Section III. The results in Section IV present both the steady validation and the characterization

of jet-buffet, including its analysis using DMD. Finally, the conclusions of the study are presented in Section V.

II. Geometric Model

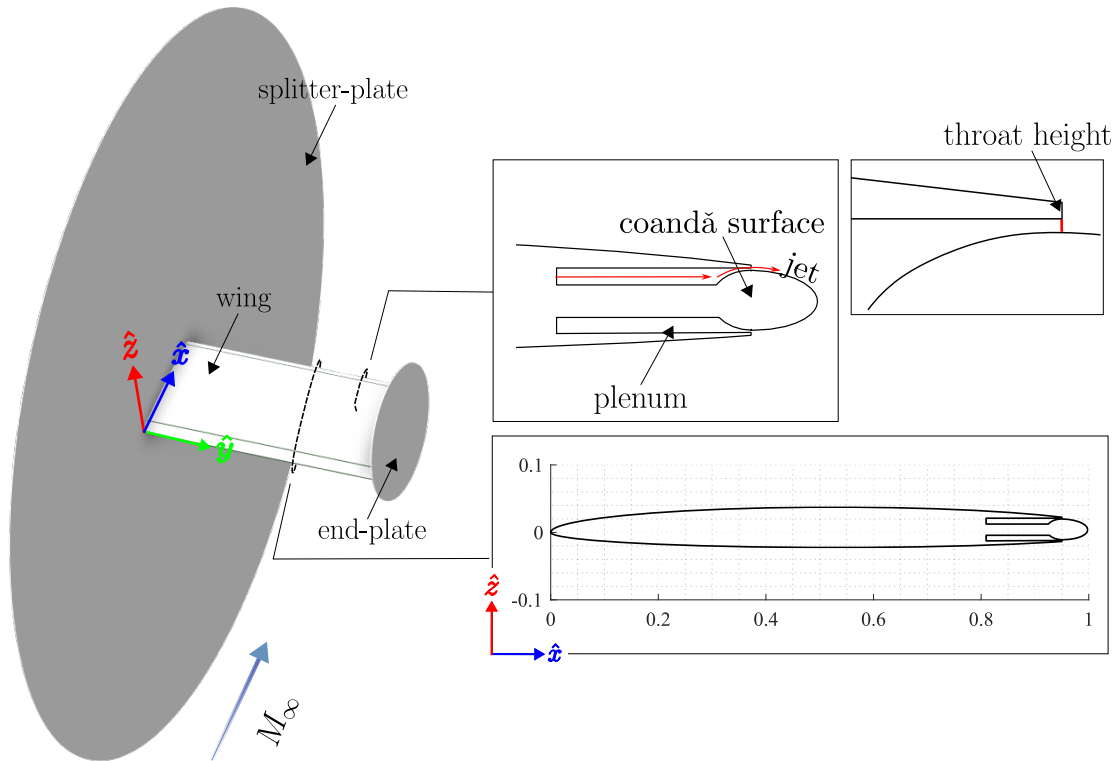


Fig. 1 Geometry of the modeled test wing

The wing cross-section used in this study, depicted in Fig. 1, is based on the geometry employed in circulation control experiments conducted at NASA's Transonic Dynamic Tunnel (TDT) [15]. It features a 6% thick elliptic airfoil with 0.75% camber and a nominal chord length of $c = 30$ inches which was used for computing aerodynamic coefficients. The actual chord length, however, was 28.5 inches due to a modification where the trailing-edge was cut at $0.9c$ and replaced with a dedicated Coandă surface. This replacement surface had an elliptic shape with a major-to-minor axis ratio of 2.98. The internal plenum, integrated within the wing, was designed to generate the jet required for circulation control. It featured a throat height of $0.012c$ and a length sufficient to produce a fully developed turbulent jet.

The test wing spanned 60 inches, corresponding to an aspect ratio of 2, and was secured in place using a splitter-plate reinforced to the tunnel wall. To mitigate three-dimensional effects, an end-plate with a diameter of one chord in length was initially attached to the wingtip. However, numerical validations [19, 21, 33] conducted for transonic circulation control research, along with the author's prior comparisons with preliminary calculations of the two-dimensional geometry, revealed that both the end-plate and splitter-plate significantly contributed to 3D effects. These effects were observed to influence the strength and position of the upper surface shock at the free-stream Mach number of $M_\infty = 0.8$.

To account for these influences, both the end-plate and splitter-plate were explicitly modeled and their dimensions were selected based on previous numerical studies [21], with values of $1.1c$ and $6c$, respectively. The computational domain was represented as a cylindrical volume with a diameter of $10c$ extending $7c$ in the spanwise direction. To ensure accuracy, the numerical study was validated against the earlier stated experiment at the TDT, which was selected due to its comprehensive dataset covering a wide range of Mach numbers M , angles of attack α , and jet momentum inputs.

III. Numerical Verification

A. Computational Grid

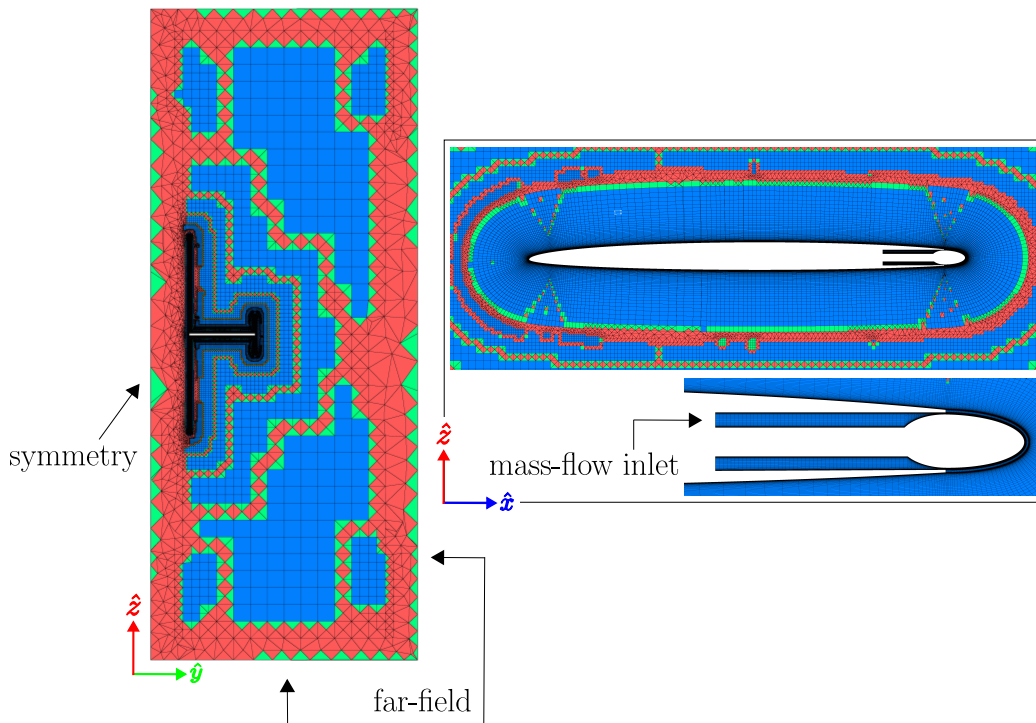


Fig. 2 Computational domain illustrating the relevant boundary conditions and cross-sections of the grid.

The computational domain was constructed using an unstructured mesh generated with Fidelity[®] Pointwise, employing the *Voxel* algorithm. This resulted in a hybrid grid comprising hexahedral and tetrahedral cells, as illustrated in Fig. 2, which depicts some of the grid's cross-sections and associated boundary conditions. To study the effects of the grid while accurately capturing the underlying flow physics, an initial fine mesh consisting of 40×10^6 cells was utilized, and subsequently coarsened up to 13×10^6 cells. Across all grid configurations, the boundary layer was resolved using 80 layers growing at a rate of 1.1, while ensuring the first cell height corresponded to $y^+ \approx 1$. Four grid variants were developed, focusing on enhanced cell density near the wing, splitter-plate, end-plate, and near-wake regions. For each grid, the mid-span lift coefficient and drag coefficient were computed and compared. Grid convergence was deemed achieved when the variation in these aerodynamic coefficients was within $O \leq 1\%$. The final grid, consisting of 28×10^6

cells, was used for the remainder of the study.

B. Numerical Setup

The computational study was conducted using Ansys[®] Fluent simulation software by solving the Reynolds Averaged Navier-Stokes (RANS) equations. Boundary conditions were set to replicate the experimental tunnel conditions from [15] with free-stream Mach number of $M_\infty = 0.8$, static pressure $p_\infty = 13789.5$ (Pa) and temperature $T_\infty = 308.15$ (K) corresponding to a free-stream chord-based Reynolds number of 3×10^6 . The jet flow from the plenum was modeled as a mass-flow inlet boundary condition, determined by the required momentum coefficient $C_\mu = \dot{m} v_j / Q_{\text{dyn}} c$, where \dot{m} is the mass-flow to the plenum, Q_{dyn} is the free-stream dynamic pressure and v_j is the isentropic jet velocity calculated by the expansion of the jet to the free-stream and defined as:

$$v_j = \sqrt{2R_g T_{0,p} \left(\frac{\gamma}{\gamma - 1} \right) \left(1 - \left(\frac{p_\infty}{p_{0,p}} \right)^{\frac{\gamma-1}{\gamma}} \right)} \quad (1)$$

where R_{gas} is the specific gas constant, γ is the specific heat capacitance ratio and $T_{0,p}$, $p_{0,p}$ are the total temperature and total pressure at the plenum respectively. To maintain consistency with the experimental definition of the lift coefficient, c_l , the pressure was integrated along the mid-span of the wing:

$$c_l = \frac{1}{c} \int_0^c (C_{p,\text{low}} - C_{p,\text{up}}) dx \quad (2)$$

Where $C_{p,\text{up}}$ and $C_{p,\text{low}}$ are the upper and lower surface pressure coefficients respectively.

For the numerical schemes, the inviscid fluxes were discretized using 2nd Roe flux difference splitting scheme and the solution gradients were computed using the Green-Gauss node based approach. Both the 2nd order Spalart-Allmaras (SA) and $k - \omega$ SST turbulence models were tested, as depicted in Fig. 3, where the pressure coefficient distribution along the mid-span chord is outlined for both turbulence models and validated against the experimental data, for the cases with no ($C_\mu = 0$), and with blowing ($C_\mu = 0.008$).

From a global perspective, CC affects the pressure profile by thickening it and shifting the upper surface shockwave further aft, as shown in Fig. 4 for the Mach field with the SA turbulence model. However, discrepancies were observed between numerical predictions and experimental data regarding the shockwave position for both turbulence models, particularly in the $C_\mu = 0.008$ case. And it is noted that the $k - \omega$ SST model showed a slightly smaller deviation. It has been suggested that this misalignment is likely due to limitations inherent to the RANS turbulence framework [21]. Since the experimental setup produced a turbulent boundary layer via an epoxy based trip strip located at 5%*c* from the leading-edge which was not geometrically modeled.

Focusing on the trailing-edge region, the calculations captured the primary effects of CC on the pressure coefficient

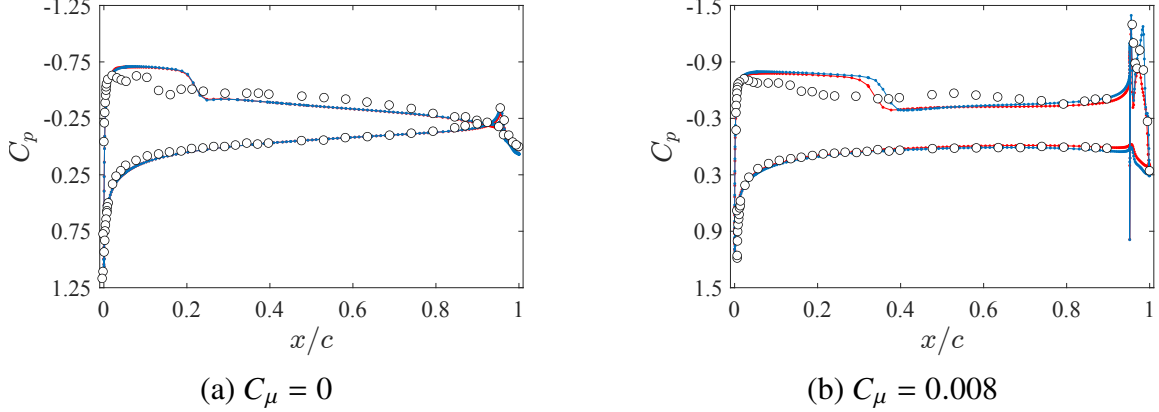


Fig. 3 Pressure coefficient distribution at mid-span for both the Spalart-Allmaras and $k - \omega$ SST models, validated against the experimental data at a free-stream Mach number of 0.8 and angle of attack of 3° . Where: (○) experimental results; -.- SA; -.- SST)

distribution as illustrated in Fig. 5 depicting both the pressure distribution along the trailing-edge in Fig. 5a as well as its corresponding Mach field in Fig. 5b. With the addition of blowing, the pressure distribution on the trailing-edge is modified by an addition of two distinct peaks (highlighted by a black box in Fig. 5b), which are a consequence of the high velocity jet. This increase in pressure is associated with the formation of a separation bubble. The first peak, located near the plenum outlet (located at $0.95 \geq x/c \leq 0.96$) showed a sharper drop than the experimental data. Although no visual data from the report are available, a sharper drop indicates a shorter bubble and thus a misrepresentation by numerical results of the bubble's length. In contrast, the second peak (located at $0.965 \geq x/c \leq 0.99$) was more accurately captured by the SA model. Since the $k - \omega$ SST overly smoothed the solution. Consequently, the Spalart-Allmaras model was selected for the remainder of the study due to its performance in accurately resolving the trailing-edge flow features.

IV. Results & Discussion

In circulation control, subsonic studies have shown that the influence of the momentum coefficient on the wing's lift can be separated from the effects of the angle of attack under pre-stall conditions [34]. This relationship can be expressed as:

$$c_l = \frac{\partial c_l}{\partial \alpha} \Delta \alpha + \frac{\delta c_l}{\delta C_\mu} \Delta C_\mu \quad (3)$$

where $\delta c_l / \delta C_\mu \approx \Delta c_l / C_\mu$ represents the augmentation ratio. While the behavior of the augmentation ratio at transonic Mach numbers remains unclear, some studies [35] have provided insights into its correlation with the momentum coefficient. Specifically, for subsonic conditions with low momentum inputs, the augmentation ratio was observed to remain constant when circulation control is maintained. This finding aligns with the trends shown in Fig. 6

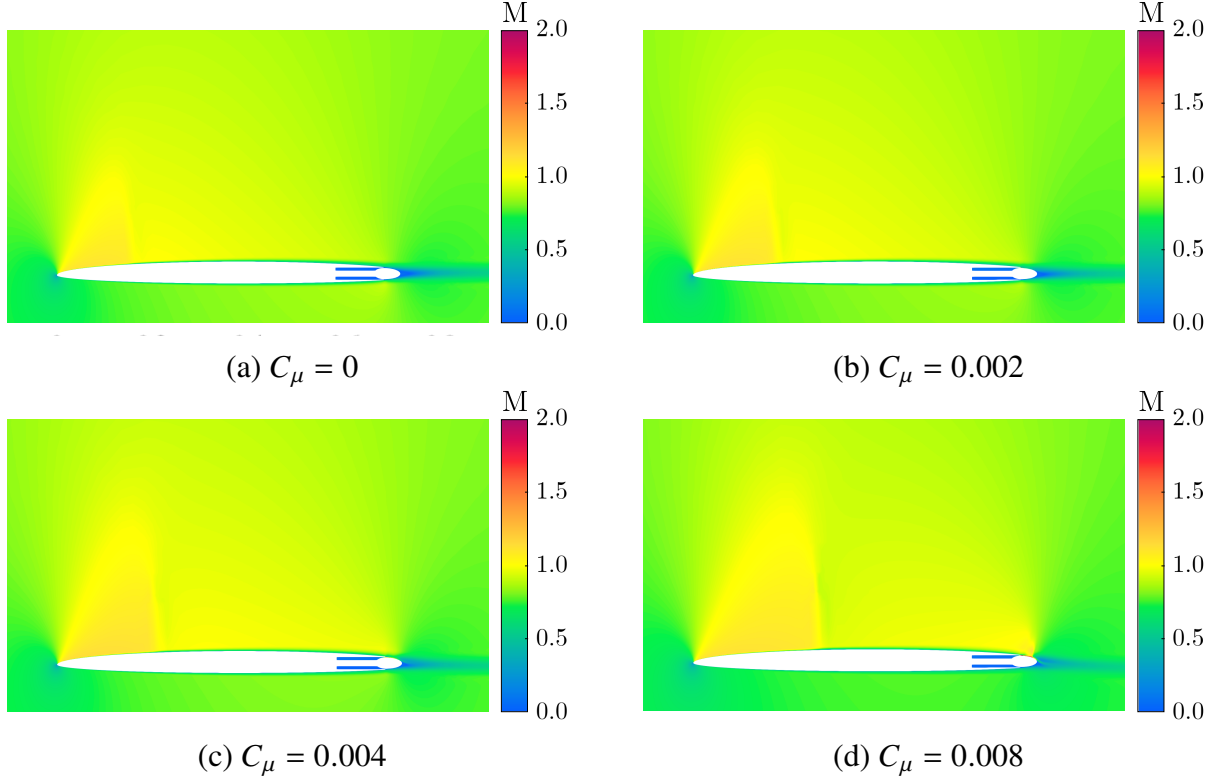


Fig. 4 Mach field at mid-span using the Spalart-Allmaras model, at a free-stream Mach number of 0.8 and angle of attack of 3° .

(for momentum inputs of $0.003 \leq C_\mu \leq 0.008$), which illustrates the variation of both the augmentation ratio and lift as functions of the momentum coefficient at an angle of attack of 3° . These results include both experimental data and numerical simulations.

When the momentum input increases beyond a certain threshold, the jet loses its authority, detaches from the surface, and the augmentation ratio rapidly declines to zero with increasing jet strength. For the lift coefficient, a noticeable plateau is observed before this rapid drop occurs. In this region (at momentum inputs of $C_\mu \geq 0.008$), attempts to achieve a steady-state solution revealed unsteady behavior in both the aerodynamic coefficients and the residuals. Similar observations were made in other studies [19, 21], although no detailed explanation was provided for this phenomenon.

A. Unsteady Flow-Field Description

To evaluate the unsteadiness, 2nd order Unsteady Reynolds-Averaged Navier-Stokes (URANS) simulations were performed at a momentum coefficient of 0.01, corresponding to the first value of the lift plateau. The results were validated through a time step sensitivity study, which considered three different time increments: $\Delta t = (1 \times 10^{-2}, 5 \times 10^{-3}, 1 \times 10^{-3})$ (ms), equating to (128, 256, 1500) iterations per cycle, respectively. Convergence was assessed based on a three-order-of-magnitude reduction in residuals per time step, as well as the stabilization of the lift coefficient's amplitude and frequency, determined via a one-sided Fast Fourier Transform (FFT). Among the tested

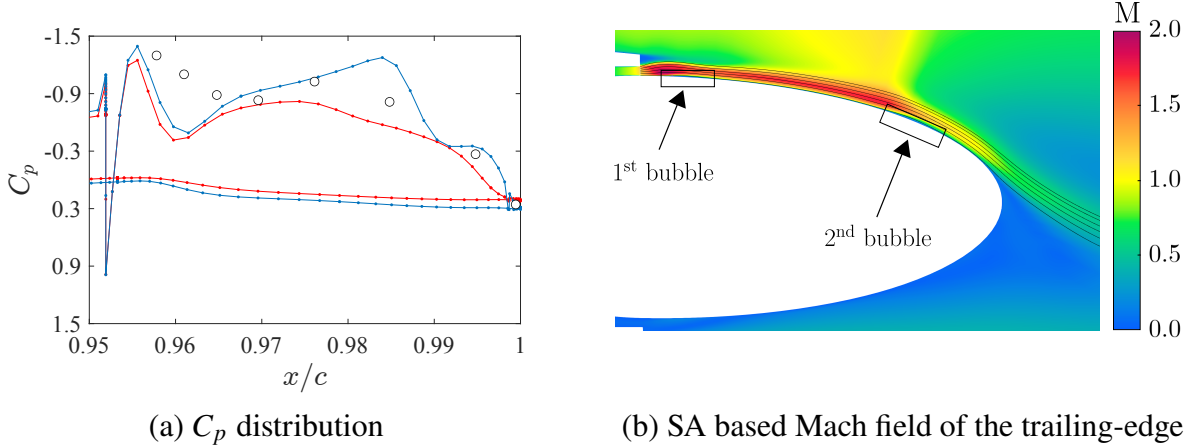


Fig. 5 Validation of the turbulence models at the trailing-edge at Mach number of 0.8, angle of attack of 3° and momentum coefficient of 0.008.

Where: (\circ) experimental results; $-\cdot-$ SA; $- \cdot -$ SST)

time increments, $\Delta t = 5 \times 10^{-3}$ (ms) was deemed sufficient for convergence, yielding a lift coefficient amplitude of 0.032 and a reduced frequency $\kappa = f_{\text{jet}} r_e / v_j$ of 0.068. Here, f_{jet} denotes the jet shedding frequency, while r_e was approximated as the major radius of the ellipse for simplicity.

An analysis of the flow-field behavior near the trailing-edge indicates that the observed unsteadiness results from periodic detachment of the jet. This phenomenon is illustrated in Fig. 7, where Mach fields are depicted for a portion of a single shedding cycle at various normalized time steps, defined as $\tau = (t - t_{c,0})/T$. Here, t represents the physical flow time, $t_{c,0}$ denotes the initial time of the detachment cycle, and T corresponds to the period. Each image in the figure thus represents the relative temporal position of the Mach fields within the cycle.

Starting from Fig. 7a ($\tau = 0$), which corresponds to the maximum lift coefficient ($c_l = 0.616$), the jet gradually begins to detach from the surface. This progression is observed in Figs. 7(b-d), culminating in full detachment at the minimum lift coefficient ($c_l = 0.581$ at $\tau = 0.23$). Reattachment initiates at $\tau = 0.31$, during which the lift coefficient gradually increases (Figs. 7(e-h)), ultimately returning to its peak value, marking the completion of the cycle.

The detachment phase of the cycle is marked by the interaction between the jet and the trailing-edge shockwave, which weakens as the cycle progresses, as well as the interaction between the jet and the underlying boundary-layer. At $\tau = 0$, the unsteady field lacks the second pressure peak or separation bubble previously discussed (see Sec. III) for momentum coefficients at the onset of periodic separation ($C_\mu = 0.008$). Typically, the separation bubble facilitates mixing between the free-stream momentum and the boundary-layer, thereby delaying detachment [36]. Consequently, its absence can lead to premature separation. In the spatial region where the bubble is present in the steady flow field, the unsteady field instead exhibits a structure formed by the interaction of the shockwave with the boundary-layer. The high-velocity jet pushes the separation bubble closer to the tip of trailing-edge, preventing its stable formation. However, sustaining a periodic cycle of separation and reattachment requires a feedback mechanism. Thus, the unsteady

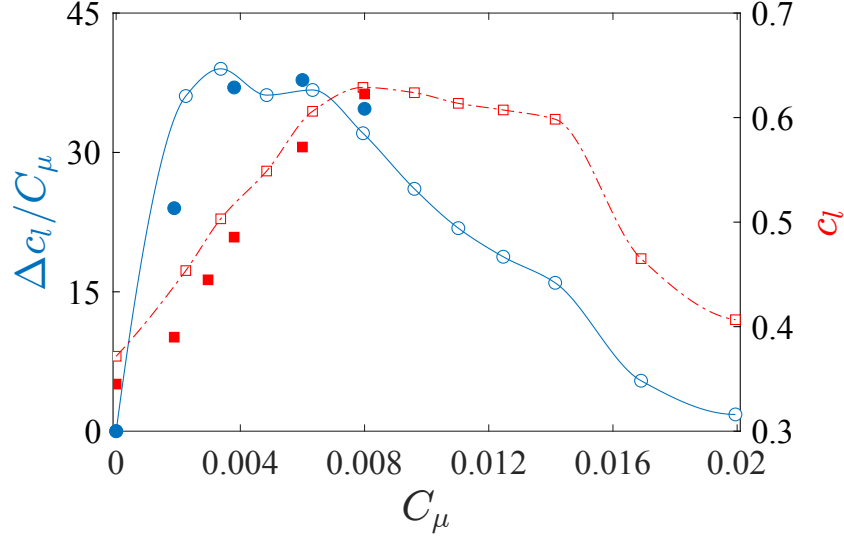


Fig. 6 Effect of C_μ on the augmentation ratio and mid-section lift at Mach 0.8 and an angle of attack of 3° . Where for $\Delta c_l / C_\mu$: (● CFD ; ○ Experiment). And for c_l : (■ CFD -□- Experiment).

solution alone does not clarify why periodicity is maintained rather than leading to complete jet detachment from the trailing-edge.

RANS computations do not directly resolve the turbulent eddies responsible for mixing, making it difficult to study the "jet-buffet" phenomenon from the perspective of the separation bubble itself. However, previous studies on periodic mechanisms at transonic speeds [27–29] (see Sec. I) indicate that the harmonic motion is primarily governed by pressure propagation. Moreover, since circulation control (CC) is predominantly a pressure-driven phenomenon [37], further insights into the jet-buffet can be obtained by analyzing the problem from a pressure-based perspective. As a result, the coupling between a primarily pressure-driven effect and periodic motion suggests that this phenomenon can be effectively analyzed using a dynamics-based approach, such as data-driven methods like Dynamic Mode Decomposition (DMD). DMD extracts the spatial-temporal modes of the flow field while relating them to the system's dynamic quantities, providing deeper insights into the origins of the phenomenon.

B. Dynamic Mode Decomposition

The modal analysis of the jet-buffet phenomenon is performed using the Dynamic Mode Decomposition (DMD) algorithm. DMD is a data-driven approach for analyzing flow-fields, combining elements of Proper Orthogonal Decomposition (POD) and the Fourier Transform [26]. Like similar techniques, it utilizes Singular Value Decomposition (SVD), a general dimensionality reduction method designed to identify low-dimensional patterns within data [25]. In the context of the observed unsteadiness, DMD serves as a dimensionality reduction tool to capture and investigate the dominant coherent structures that appear to form the jet-buffet. To achieve this, the mean-reduced pressure field is structured into the matrix $X \in \mathbb{R}^{n \times m}$, where the number of rows, n , represents the spatial locations of pressure values,

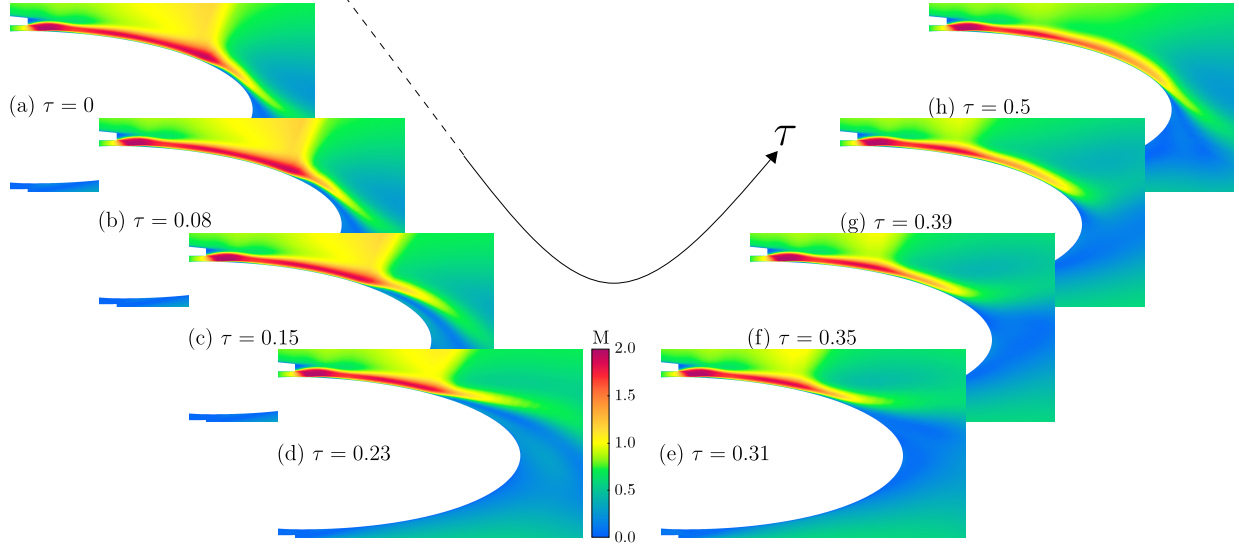


Fig. 7 Mach fields of the mid-span depicting the vortex shedding evolution from the trailing-edge. With a momentum coefficient of 0.01 at angle of attack of 3° , and free-stream Mach of 0.8.

and the number of columns, m , corresponds to the discrete time steps.

The formal mathematical derivation [25] states that if $X \in \mathbb{C}^{n \times m}$ is a matrix where $n \gg m$, then using Singular Value Decomposition (SVD), X can be decomposed into the left singular matrix, also known as the POD modes, $\Psi \in \mathbb{C}^{n \times n}$, which optimally describes X in a least-squares sense [38], and the right singular matrix $V \in \mathbb{C}^{m \times m}$, both of which are unitary, satisfying $\Psi\Psi^* = \Psi^*\Psi = I$ and $VV^* = V^*V = I$, where the superscript $()^*$ denotes the conjugate transpose. These matrices satisfy the eigenvalue equation $XV = \Psi\Sigma$, where $\Sigma \in \mathbb{C}^{n \times m}$ is a diagonal matrix containing the data set's singular values arranged in descending order. To obtain a low-rank approximation, a practical approach involves using the "economy" SVD, which removes the zero-valued elements of Σ . This leads to the reduced form $X = \hat{\Psi}\hat{\Sigma}\hat{V}^*$, where $\hat{\Psi} \in \mathbb{R}^{n \times r}$, $\hat{\Sigma} \in \mathbb{R}^{r \times r}$, $\hat{V} \in \mathbb{R}^{r \times m}$, and $r \leq \min(m, n)$.

The DMD algorithm seeks to determine the matrix A that propagates the snapshots of X forward in time, such that $X' \approx AX$, where X' represents X advanced by one time step. In a least-squares sense, A is obtained by solving the minimization problem $\|X' - AX\|_F$, where $\|\cdot\|_F$ denotes the Frobenius norm. Consequently, the non-linear dynamics of the system are approximated linearly through the matrix A . The dynamic modes, or DMD modes, Φ , are the eigenvectors of A , associated with the eigenvalues $\Lambda \in \mathbb{C}$, where the diagonal elements $\Lambda_{jj} = \lambda_j$ represent the continuous-time eigenvalues. These eigenvalues are mapped as $\lambda = \ln(\mu)/\Delta t$, where μ denotes the discrete-time eigenvalues of A . Using this relation, the system's linearized modal frequencies and decay rates can be determined by $f = \text{img}(\ln(\mu))/2\pi\Delta t$ and $\xi = \text{real}(\ln(\mu))/\Delta t$ respectively. For a second-order linear system, the natural frequency f_n and the damping ratio ζ are related to λ through the equation:

$$\lambda = -2\pi f_n \zeta + i2\pi f_n \sqrt{1 - \zeta^2} \quad (4)$$

From this, the natural frequency and damping ratio can be computed as $f_n = |\lambda|/2\pi$ and $\zeta = -\xi/f_n$.

In practice, the modes and frequencies are determined by projecting the matrix A onto the Proper Orthogonal Decomposition (POD) modes [26]. This is expressed as $\tilde{A} = \Psi^* A \Psi$, which utilizes the Singular Value Decomposition (SVD), leading to $\tilde{A} = \Psi^* X' V \Sigma^{-1}$. The matrix \tilde{A} shares the same eigenvalues as A and provides a partial approximation of its eigenvectors. Using the eigendecomposition of \tilde{A} , the eigenvectors W are employed to reconstruct the dynamic modes as $\Phi = X' V \Sigma^{-1} W$. As a result, the continuous-time solution is expressed as:

$$x(t) \approx \sum_{j=1}^r \phi_j e^{\lambda_j t} b_j \quad (5)$$

where $b = \Phi^{-1} x(t_0)$ represents the modal amplitude.

1. Preliminary Modal Analysis

The DMD process begins by identifying the dominant modes necessary to accurately capture the jet-buffet phenomenon. By mapping the eigenvalues of A onto the complex plane, as shown in Fig. 8(a), periodicity can be assessed, allowing for the identification of modes associated with the jet-buffet. The data reveals that the eigenvalue distribution on the unit circle contains a cluster of values near $\text{img}(\mu) = 0$, where the decay approaches 1 (marked in red in Fig. 8(a)). These eigenvalues correspond to low natural frequencies. Specifically, the eigenvalue $\mu_{\text{jet}} = 0.9995 + 0.0244i$ corresponds to a natural frequency of $f_{\text{jet}} = 777.86$ Hz or $\kappa = 0.062$, which is consistent with the reduced frequency obtained from the prior FFT analysis. This eigenvalue aligns with the third and fourth modes (ordered by natural frequency) and is under-damped, with a damping ratio of $\zeta_{\text{jet}} = 0.00621$, indicating a periodically stable system.

Based on this observation, the relationship of each mode to the jet-buffet can be identified by examining the linear dependence of the natural frequencies, normalized by the obtained buffet frequency f_{jet} (Fig. 8b). Similar studies [28] found that when this dependency breaks, the corresponding modes become disassociated from the dynamic phenomenon. In the present case, the linearity holds for all modes, as no other dynamic effects are present in the accumulated flow-field data. To assess the contribution of these modes to the jet-buffet, a low-rank approximation is made based on their influence on the flow-field, such as through the modal influence [39], which is defined as:

$$I_k = \sum_{j=1}^k b_j \|\lambda_j\|$$

The modal influence accounts for both the modal amplitude b (depicted independently in Fig. 8c) and the decay rate ξ . As shown in Fig. 8(d), capturing 99.9% of the modal influence requires tens to hundreds of modes, in part due to weakly energetic effects that have a significant impact on the dynamics. These effects are given greater weight through the modal influence because of their contribution to the amplitude.

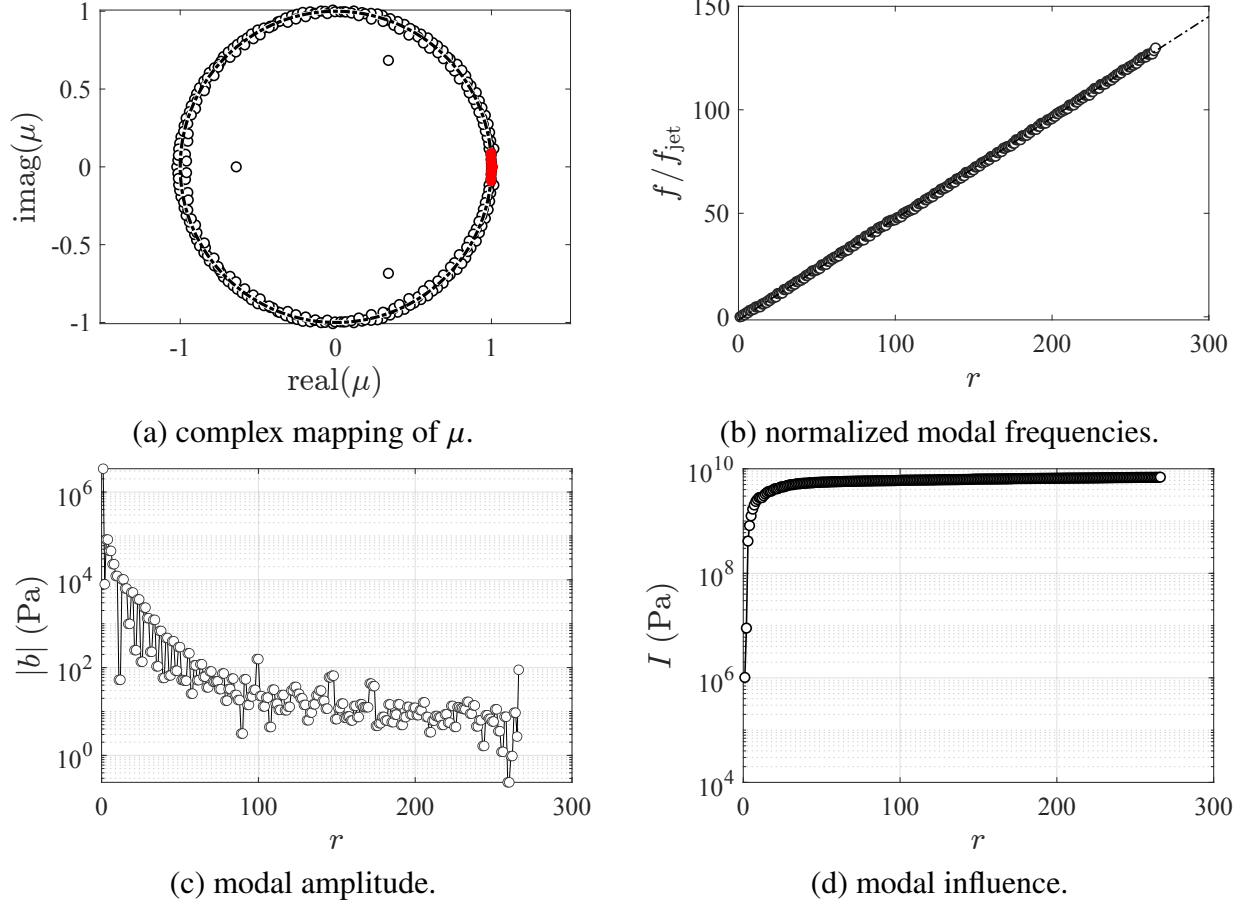


Fig. 8 Results of the preliminary analysis conducted to ascertain the jet-buffet mode.

2. Modal Decomposition

Figure 9 shows the normalized spatial amplitude $|\tilde{\Phi}| = |\Phi/\max(\Phi)|$ of both the first mode, which corresponds to the steady flow-field, and the first modal pair ($r = 3, 4$), which not only relates to the jet-buffet frequency but also has the highest modal amplitude among the buffet modes. As previously noted, increasing the jet momentum causes the upper surface shockwave to move further aft. From Fig. 9(a,c), it can be seen that while the upper surface shock is present in the first mode, it is absent in the modal pair and in subsequent modes. This absence is due to the jet's inability to continue augmenting the circulation of the wing and as a result, cannot further shift the shock's position. Therefore, it is understood that jet-buffet marks the end of circulation control, even prior to complete jet separation.

Also noted is a pressure structure seen on the surface of the trailing-edge at $r = 3, 4$ in Fig. 9d, which extends above the surface and contains a pressure core characterized by large gradients from its center, as well as a smaller pressure bubble further downstream. These structures match in form to the interaction of the trailing-edge shock with the unstable separation bubble.

Superseding the latter modes are those shown in Fig. 10 in terms of their normalized spatial distribution. These

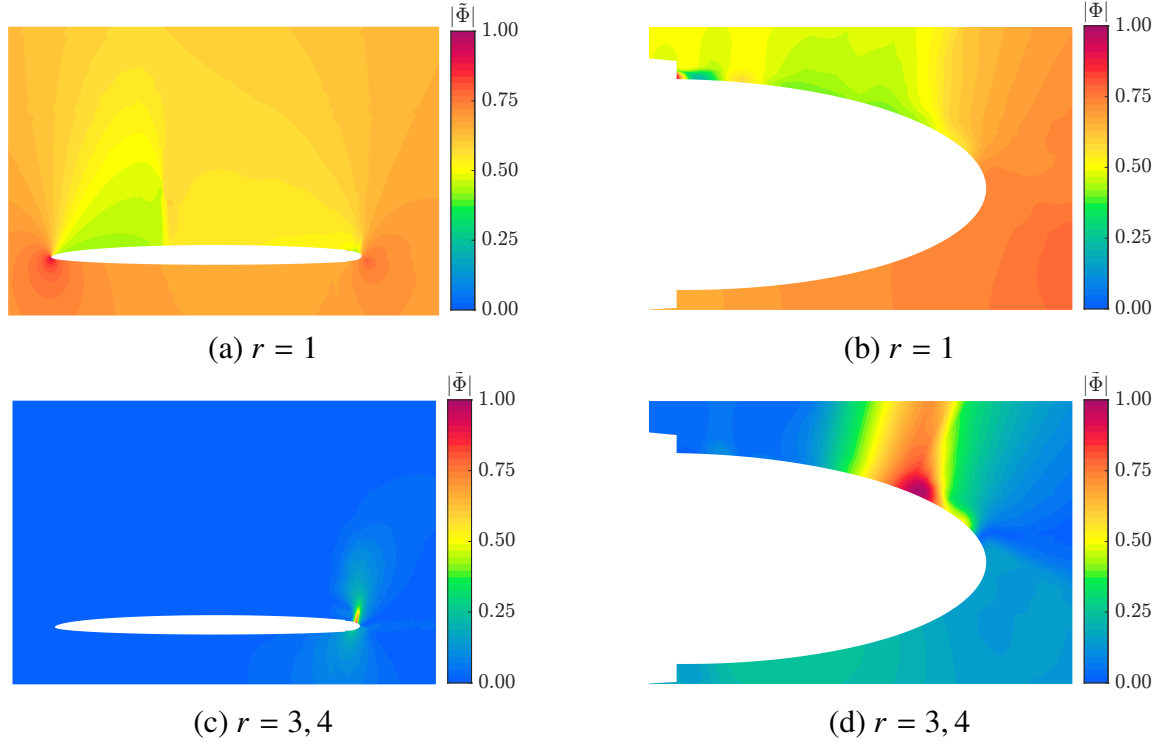


Fig. 9 Spatial distribution field of the first steady and unsteady modes.

modal pairs account for 44% of the modal influence and exhibit a maximal difference in modal amplitude of order $\mathcal{O}(10^4)$. As the mode number increases, the spatial contribution decreases. The pressure structure first observed at $r = 3, 4$ becomes fragmented as the mode number increases, separating into an individual shock structure and a small pressure bubble. Meanwhile, its high-amplitude core steadily rises above the surface of the trailing-edge. The pressure bubble advances along the trailing-edge until it is shed into the wake, while the shock is gradually weakened and detached. When the higher modes are reached $r = 11, 12$ in Fig. 10e, the shock structure is completely detached, and the bubble is no longer visible. The initial formation and its fragmentation at increasing modal numbers suggest that the unsteady field is influenced by both the combined shock-pressure bubble and their individual components. The subsequent dissipation of both components indicates that above a certain mode number, the effects of the jet-buffet are diminished, and other effects, such as the shedding itself, become dominant. Furthermore, the initial structure observed in the first modal pair is no longer visible as we progress through the different modes. Therefore, it is understood that the fragmentation of the initial structure is the driving mechanism behind the jet-buffet cycle.

Additional information on the driving mode can be obtained by examining its phase shift ϕ_Φ , as shown in Fig. 11. Based on the phase contribution from the complex spatial distribution, i.e., $\Phi = |\Phi|e^{i\phi_\Phi}$, the analysis of the spatial phase allows us to pinpoint the direction of the pressure waves by tracing the shift from positive to negative values. Notably, in Fig. 11a, the phase shift indicates that the pressure wave moves from the leading-edge downstream to the

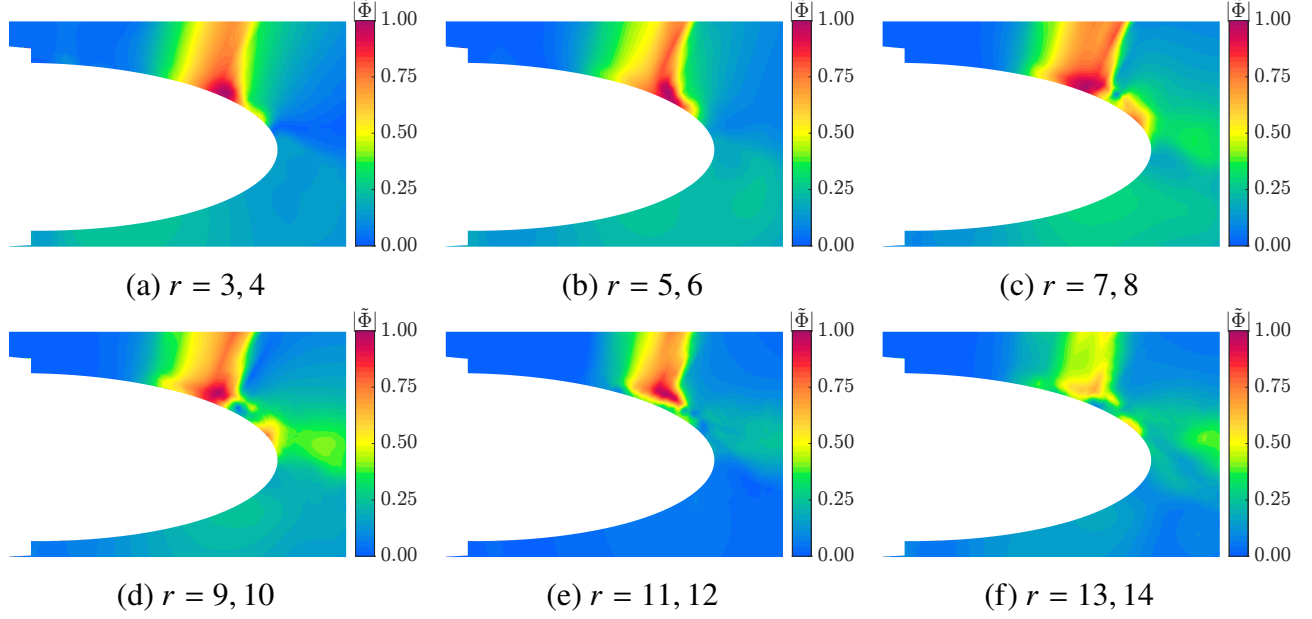


Fig. 10 Spatial distribution of the first six modal pairs.

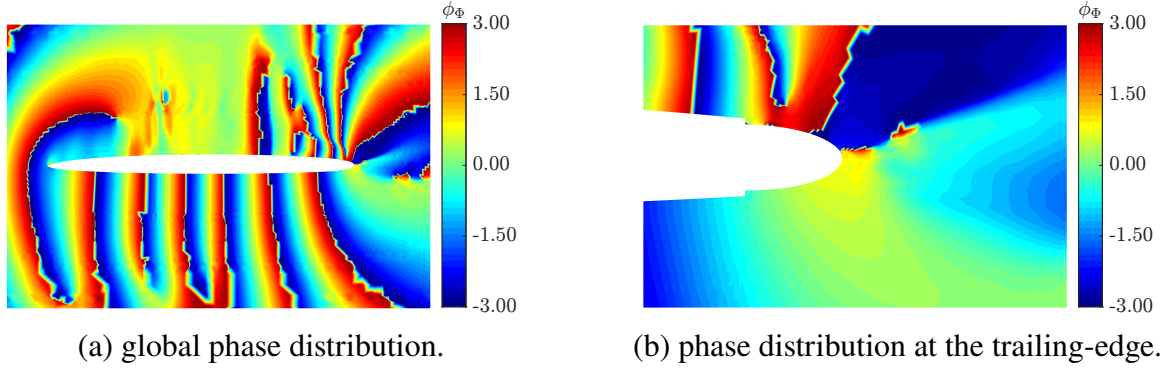


Fig. 11 Phase of the spatial distribution for $r = 3, 4$.

trailing-edge, from the underside of the wing. Similarly, on the upper surface, the wrapping of the phase distribution around the leading-edge and the sudden bi-directional movement of the pressure waves some distance from it depict the upper surface shock. Regardless of its absence previously due its negligible spatial distribution magnitude. Further downstream, the presence of the trailing-edge shockwave compresses the pressure waves, resulting in a smaller spacing of the phase shift. When focusing on the trailing-edge (Fig. 11b), small regions are observed some distance away from its where the phase shift is reversed, indicating pressure propagation traveling upstream. Although the origin of this upstream propagation is difficult to ascertain from the phase distribution alone.

Based on the previous observation, the time development and contribution to the pressure reconstruction of the driving mode, i.e., $p_3 = b_3\Phi_3e^{\lambda_3 t}$, can be examined, as shown in Fig. 12, for different pressure distributions along the jet-buffet cycle. Where $\tau = 0, 1$ correspond to the reconstructed maxima of the single mode. During these times,

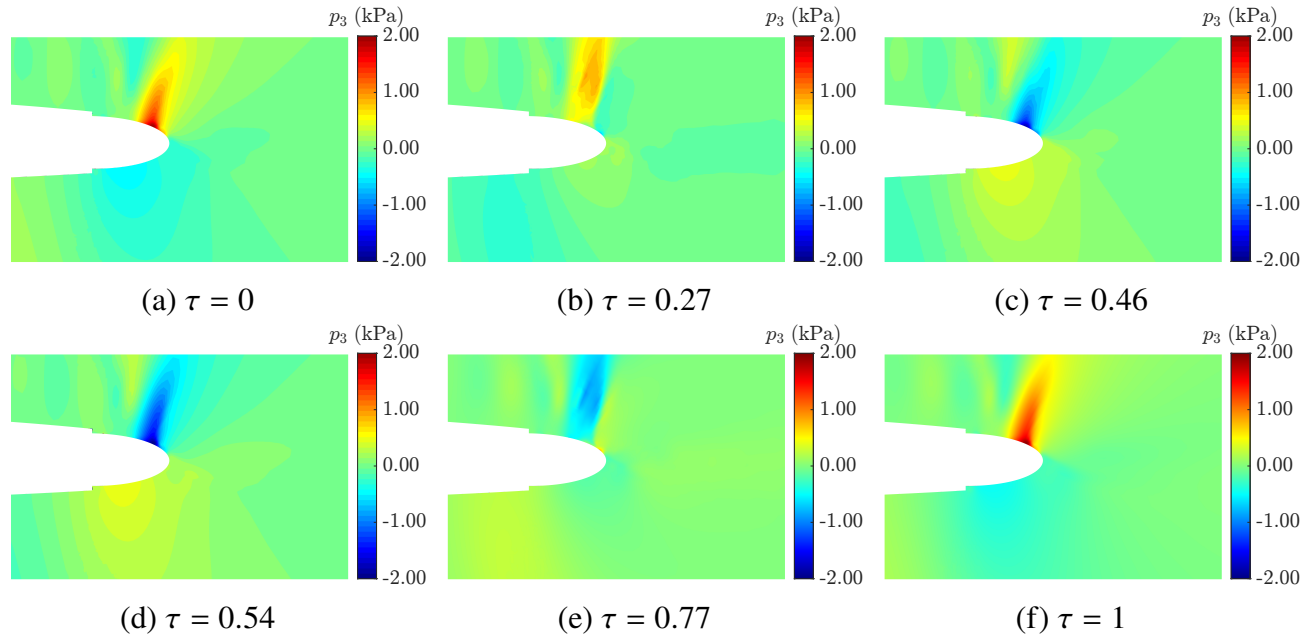


Fig. 12 Time development of the pressure field, reconstructed using the first modal pair $r = 3, 4$.

the high amplitude of the shock-bubble structure on the trailing-edge has a positive sign due to the jet attachment. Meanwhile, at $\tau = 0.46, 0.54$, the combined structure has a negative sign due to the jet detachment. Additionally, $\tau = 0.27, 0.77$ represent the points in the cycle where the trailing-edge pressure structure shifts its phase. As further illustrated in Fig. 13 it is observed that when the phase shifts, the pressure bubble is in anti-phase with the shock formation which subsequently separates from the trailing-edge surface. Thus, the driving mechanism of the jet-buffet relies on the feedback from the bubble downstream. As the cycle progresses, pressure waves propagate from the pressure bubble to the shock formation and vice versa, causing an interference that detaches and reattaches the shock to the surface, thus creating the jet-buffet.

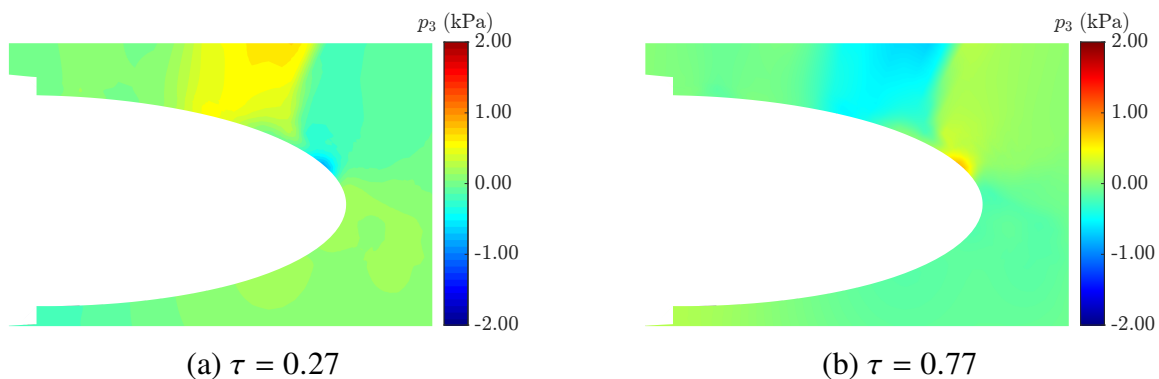


Fig. 13 Reconstructed pressure using $r = 3, 4$ at the temporal location where phase shift occurs between the pressure bubble and the shock formation.

V. Conclusions

A numerical validation via RANS was performed for an experimental study investigating the applications of circulation control (CC) on an elliptic airfoil at transonic conditions. The steady-state results aligned well with the experimental study, matching the pressure distribution and capturing the major effects, such as the upper surface shock and trailing-edge separation bubble, albeit with slight inconsistencies in their locations.

Upon assessing the contribution of CC at higher momentum coefficients ($C_{\mu} = 0.01$), unsteadiness was observed, as seen in previous studies, prompting the use of a URANS simulation to investigate its impact on the flow-field. The analysis revealed an interaction between the high-momentum jet, the trailing-edge shock, and the separation bubble, which caused the bubble to disperse. This interaction induced oscillations in the lift coefficient, a phenomenon referred to as the jet-buffet. Further investigation through Dynamic Mode Decomposition (DMD) revealed that the jet-buffet dynamics were largely decoupled from the upper surface shock. This decoupling resulted from the inability of the jet to further augment the wing's circulation, preventing the wing from conforming to super-circulation.

The origin of the jet-buffet was explored through the dynamic modes obtained via DMD analysis. It was determined that the phenomenon is driven by the formation of a shock-bubble structure, with a distinct pressure core at its center. As the modes progressed, the structure fragmented, producing higher-order modes in which the pressure bubble moved along the trailing-edge before being shed into the wake.

The time development of the driving mode further elucidated its origins. As the cycle progressed, pressure propagation between the shock and separation bubble caused interference, resulting in shock detachment from the surface. This mechanism was responsible for both the detachment and subsequent reattachment of the jet.

The implications of these findings suggest that while the jet-buffet leads to the degradation of the CC mechanism under these conditions, it could also result in structural oscillations and impose a significant cost to the wing's stability due to rapidly changing wing moments. Thus, the presence of the jet-buffet could influence the practical application of CC for transonic flight.

References

- [1] Yarf-Abbasi, A., and Fielding, J., "Design Integration of the Eclipse and Demon Demonstrator UAVs," *7th AIAA Aviation Technology Integration and Operations Conference (ATIO)*, American Institute of Aeronautics and Astronautics, 2007. <https://doi.org/10.2514/6.2007-7725>.
- [2] Crowther, W. J., Wilde, P. I. A., Gill, K., and Michie, S. M., "Towards Integrated Design of Fluidic Flight Controls for a Flapless Aircraft," *The Aeronautical Journal*, Vol. 113, No. 1149, 2009, pp. 699–713. <https://doi.org/10.1017/S0001924000003365>.
- [3] Warsop, C., and Crowther, W. J., "Fluidic Flow Control Effectors for Flight Control," *AIAA Journal*, Vol. 56, No. 10, 2018, pp. 3808–3824. <https://doi.org/10.2514/1.J056787>.

- [4] Warsop, C., and Crowther, W., “NATO AVT-239 Task Group: Flight Demonstration of Fluidic Flight Controls on the MAGMA Subscale Demonstrator Aircraft,” *AIAA Scitech 2019 Forum*, American Institute of Aeronautics and Astronautics, 2019. <https://doi.org/10.2514/6.2019-0282>.
- [5] Montoro, J., Carbaugh, W. L., and Miller, D. N., “DARPA CRANE Program Overview by Lockheed Martin,” *AIAA Scitech 2023 Forum*, American Institute of Aeronautics and Astronautics, 2023. <https://doi.org/10.2514/6.2023-1808>.
- [6] McVeigh, M. A., Nagib, H., Wood, T., and Wygnanski, I., “Full-Scale Flight Tests of Active Flow Control to Reduce Tiltrotor Aircraft Download,” *Journal of Aircraft*, Vol. 48, No. 3, 2011, pp. 786–796. <https://doi.org/10.2514/1.46956>.
- [7] Lin, J. C., Andino, M. Y., Alexander, M. G., Whalen, E. A., Spoor, M. A., Tran, J. T., and Wygnanski, I. J., “An Overview of Active Flow Control Enhanced Vertical Tail Technology Development,” *54th AIAA Aerospace Sciences Meeting*, American Institute of Aeronautics and Astronautics, 2016. <https://doi.org/10.2514/6.2016-0056>.
- [8] Keisar, D., Hasin, D., and Greenblatt, D., “Plasma Actuator Application on a Full-Scale Aircraft Tail,” *AIAA Journal*, Vol. 57, No. 2, 2019, pp. 616–627. <https://doi.org/10.2514/1.J057233>.
- [9] Polonsky, D., Stalnov, O., and Greenblatt, D., “Noise Reduction on a Model Helicopter Rotor Using Dielectric Barrier Discharge Plasma Actuators,” *AIAA Journal*, Vol. 61, No. 7, 2023, pp. 3134–3141. <https://doi.org/10.2514/1.J062626>.
- [10] Polonsky, D., Oksana, S., and Greenblatt, D., “Battery-Powered Helicopter Hover Performance Enhancement Using DBD Plasma Actuator,” *AIAA Aviation 2023 Forum*, American Institute of Aeronautics and Astronautics, 2023. <https://doi.org/10.2514/6.2023-4308>.
- [11] Coanda, H., “Device for Deflecting a Stream of Elastic Fluid Projected into an Elastic Fluid,” 1935. URL <https://patents.google.com/patent/US2052869A/en>.
- [12] Englar, R. J., and Williams, R. M., “Design of a circulation control stern plane for submarine applications,” Tech. rep., David W Taylor Naval ship Research and Development Center. Bethesda, MD, 1971. URL <https://apps.dtic.mil/sti/citations/tr/AD0901198>.
- [13] Giannelis, N. F., Vio, G. A., and Levinski, O., “A review of recent developments in the understanding of transonic shock buffet,” *Progress in Aerospace Sciences*, Vol. 92, 2017, pp. 39–84. <https://doi.org/10.1016/j.paerosci.2017.05.004>.
- [14] Loth, J. L., and Boasson, M., “Circulation controlled STOL wing optimization,” *Journal of Aircraft*, Vol. 21, No. 2, 1984, pp. 128–134. <https://doi.org/10.2514/3.48235>.
- [15] Alexander, M. G., Anders, S. G., Stuart, K., Florance, J. P., and Keller, D. F., “Trailing Edge Blowing on a Two Dimensional Six Percent Thick Elliptical Circulation Control Airfoi up to Transonic Conditions,” Tech. rep., NASA Langley Research Center, 2005. URL <https://ntrs.nasa.gov/citations/20050165090>.
- [16] Milholen, W. E., Jones, G. S., Chan, D. T., Goodliff, S., Anders, S., Pack Melton, L. G., Carter, M. B., Allan, B. G., and Capone, F., “Enhancements to the FAST-MAC Circulation Control Model and Recent High-Reynolds Number Testing in the National

- Transonic Facility,” *31st AIAA Applied Aerodynamics Conference*, American Institute of Aeronautics and Astronautics, 2013. <https://doi.org/10.2514/6.2013-2794>.
- [17] Milholen, W., Jones, G., and Chan, D., “High-Reynolds Number Circulation Control Testing in the National Transonic Facility,” *50th AIAA Aerospace Sciences Meeting Including the New Horizons Forum and Aerospace Exposition*, American Institute of Aeronautics and Astronautics, 2012. <https://doi.org/10.2514/6.2012-103>.
- [18] Chan, D. T., Jones, G. S., Milholen, W. E., and Goodliff, S. L., “Transonic Drag Reduction Through Trailing-Edge Blowing on the FAST-MAC Circulation Control Model,” *35th AIAA Applied Aerodynamics Conference*, American Institute of Aeronautics and Astronautics, 2017. <https://doi.org/10.2514/6.2017-3246>.
- [19] Li, Y., and Qin, N., “Airfoil Gust Load Alleviation by Circulation Control,” *Aerospace Science and Technology*, Vol. 98, 2020, p. 105622. <https://doi.org/10.1016/j.ast.2019.105622>.
- [20] Forster, M., Biava, M., and Steijl, R., “Multipoint Optimisation of Coanda Surfaces for Transonic Circulation Control Using the Adjoint Method,” *8th AIAA Flow Control Conference*, American Institute of Aeronautics and Astronautics, 2016. <https://doi.org/10.2514/6.2016-3773>.
- [21] Forster, M., and Steijl, R., “Numerical Simulation of Transonic Circulation Control,” *53rd AIAA Aerospace Sciences Meeting*, American Institute of Aeronautics and Astronautics, 2015. <https://doi.org/10.2514/6.2015-1709>.
- [22] Forster, M., and Steijl, R., “Design study of Coanda devices for transonic circulation control,” *The Aeronautical Journal*, Vol. 121, No. 1243, 2017, pp. 1368–1391. <https://doi.org/10.1017/aer.2017.65>.
- [23] Chen, Y., Hou, Z., Deng, X., Guo, Z., Shao, S., and Xu, B., “Numerical Study of the Lift Enhancement Mechanism of Circulation Control in Transonic Flow,” *Aerospace*, Vol. 8, No. 11, 2021, p. 311. <https://doi.org/10.3390/aerospace8110311>.
- [24] Englar, R. J., “Two-Dimensional Transonic Wind Tunnel Tests of Three 15-Percent Thick Circulation Control Airfoils,” Tech. rep., Defense Technical Information Center, 1970. <https://doi.org/10.21236/AD0882075>.
- [25] Brunton, S. L., and Kutz, J. N., *Data-driven science and engineering: Machine learning, dynamical systems, and control*, Cambridge University Press, 2022.
- [26] Kutz, J. N., Brunton, S. L., Brunton, B. W., and Proctor, J. L., *Dynamic mode decomposition: data-driven modeling of complex systems*, SIAM, 2016.
- [27] Santana, G. M., Fabro, A. T., and Miserda, R. F., “Analysis of the dynamic modes of the transonic flow around a cylinder,” *Journal of the Brazilian Society of Mechanical Sciences and Engineering*, Vol. 46, No. 9, 2024, p. 581. <https://doi.org/10.1007/s40430-024-05168-3>.
- [28] Poplinger, L., Raveh, D. E., and Dowell, E. H., “Modal analysis of transonic shock buffet on 2D airfoil,” *AIAA Journal*, Vol. 57, No. 7, 2019, pp. 2851–2866. <https://doi.org/10.2514/6.2021-1646>.

- [29] Liu, H., Yan, C., Zhao, Y., and Qin, Y., “Analysis of pressure fluctuation in transonic cavity flows using modal decomposition,” *Aerospace Science and Technology*, Vol. 77, 2018, pp. 819–835. <https://doi.org/10.1016/j.ast.2018.03.033>.
- [30] Koopman, B. O., “Hamiltonian systems and transformation in Hilbert space,” *Proceedings of the National Academy of Sciences*, Vol. 17, No. 5, 1931, pp. 315–318. <https://doi.org/10.1073/pnas.17.5.315>.
- [31] Kutz, J., Tu, J., Proctor, J., and Brunton, S., “Compressed sensing and dynamic mode decomposition,” *JCD*, Vol. 2, No. 2, 2016, pp. 165–191. <https://doi.org/10.3934/jcd.2015002>.
- [32] Dung, H. T. K., and Khanh, N. P., “Research on aeroelasticity phenomenon in aeronautical engineering,” *Aerodynamics*, IntechOpen, 2020. <https://doi.org/10.5772/intechopen.91748>.
- [33] Cruz, J., and Anders, S., “Assessment of an Unstructured-Grid Method for Predicting Aerodynamic Performance of Jet Flaps,” *24th AIAA Applied Aerodynamics Conference*, American Institute of Aeronautics and Astronautics, 2006. <https://doi.org/10.2514/6.2006-3868>.
- [34] Loth, J. L., “Advantages of combining BLC suction with circulation control high-lift generation,” *AIAA Journal*, 2006, pp. 3–21. <https://doi.org/10.2514/5.9781600866838.0003.0022>.
- [35] Cerchie, D., Halfon, E., Hammerich, A., Han, G., and Taubert, L., “Some circulation and separation control experiments,” *AIAA Journal*, 2006, pp. 113–165. <https://doi.org/10.2514/5.9781600866838.0113.0166>.
- [36] Greenblatt, D., and Wygnanski, I. J., “The control of flow separation by periodic excitation,” *Progress in aerospace Sciences*, Vol. 36, No. 7, 2000, pp. 487–545. [https://doi.org/10.1016/S0376-0421\(00\)00008-7](https://doi.org/10.1016/S0376-0421(00)00008-7).
- [37] Greenblatt, D., and Williams, D. R., “Flow Control for Unmanned Air Vehicles,” *Annual Review of Fluid Mechanics*, Vol. 54, No. 1, 2022, pp. 383–412. <https://doi.org/10.1146/annurev-fluid-032221-105053>.
- [38] Rowley, C. W., and Dawson, S. T., “Model reduction for flow analysis and control,” *Annual Review of Fluid Mechanics*, Vol. 49, No. 1, 2017, pp. 387–417. <https://doi.org/10.1146/annurev-fluid-010816-060042>.
- [39] Kou, J., and Zhang, W., “An improved criterion to select dominant modes from dynamic mode decomposition,” *European Journal of Mechanics-B/Fluids*, Vol. 62, 2017, pp. 109–129. <https://doi.org/10.1016/j.euromechflu.2016.11.015>.